Anatomical Based FDG-PET Reconstruction for the Detection of Hypometabolic Regions in Epilepsy

Kristof Baete, *Student Member, IEEE,* Johan Nuyts, *Member, IEEE,* Wim Van Paesschen, Paul Suetens, *Member, IEEE,* and Patrick Dupont

***Abstract*— Positron emission tomography (PET) of the cerebral glucose metabolism has shown to be useful in the presurgical evaluation of patients with epilepsy. An iterative reconstruction algorithm is derived for the detection of subtle hypometabolic regions in FDG-PET images of the brain of epilepsy patients. Prior anatomical information, derived from MR data, and pathofysiological knowledge was included in the reconstruction algorithm. Results showed an improved signal-to-noise ratio and a reduction of bias.**

***Index Terms*— Positron emission tomography, iterative reconstruction algorithm, anatomical prior information, epilepsy**

I. Introduction

PATIENTS with refractory epilepsy can be treated by surgical removal of the epileptogenic region in the brain. Positron emission tomography (PET) of the cerebral glucose metabolism in these patients has shown to be very useful in the presurgical evaluation. We derive an iterative reconstruction algorithm, dedicated for the detection of epileptogenic regions in FDG-PET images of the brain of epilepsy patients. In this algorithm, anatomical information and knowledge about the pathofysiology of the glucose metabolism in epilepsy is included.

II. Methodology

A. Assumptions

Interictal (i.e. between seizures) ^{18}FDG-PET images often show a decreased cerebral glucose metabolism in the gray matter (GM) of patients with refractory partial epilepsy. This hypometabolic region usually comes with the epileptogenic region. If no lesions or tumors can be found as the cause of epilepsy, we can assume that the metabolic activity of the white matter (WM) is uniform. Moreover, no tracer accumulation is expected in the cerebrospinal fluid (CSF) during the measurement. The identification of GM, WM and CSF can be obtained from a high-resolution anatomical MR image of the brain of the same individual. Current segmentation algorithms of the brain [1] can accurately determine the different tissue classes. The remaining unlabeled voxels are grouped in an additional class, labeled "other". In most segmentation algorithms, the procedure returns the probability that a voxel belongs to a certain tissue class. This is generally called, a fuzzy classification. For each voxel, we will assume that the probability for a tissue class approximates the underlying tissue composition. This implies that the segmentation probability is interpreted as a tissue fraction [2]. The set of segmentation images is then denoted $\{f^G, f^W, f^C, f^O\}$ and represents the a priori knowledge which will be incorporated in the reconstruction algorithm. Note that for each voxel j,

$$f_j^G + f_j^W + f_j^C + f_j^O = 1 \tag{1}$$

Differences in geometric alignment and image sampling grid are typical for images of the same patient using two imaging modalities. However, using a state-of-the-art image registration algorithm [3], it is possible to compute the affine transformation matrix $\mathcal{T}$ that is needed to align the MR image with the PET image. This action requires a preliminary reconstruction of the emission data. Since registration algorithms for the brain are very accurate, we will neglect registration errors. $\mathcal{T}$ is then used to align the segmentation images with the PET image.

B. Derivation of the algorithm

Due to a tracer activity distribution $\Lambda = \{\lambda_j \,|\, j = 1, \ldots, J\}$ in the field of view of a PET scanner, y_i photon pairs are measured at a line of response i. If λ_j represents the amount of activity at voxel position j and c_{ij} is the probability that photons emitted in voxel j were detected in i, then $E(y_i) = \sum_j c_{ij}\lambda_j$ represents the expected amount of photon pairs. The matrix of detection probabilities $\{c_{ij}\}$ is called the system matrix and contains a mathematical description of the projection process with the associated physical effects that take place between emission and detection of photons. Since, we assume that the measurements are samples from a Poisson distribution, the logarithm of the likelihood of measuring y_i, when $E(y_i)$ is expected, is

$$L = \sum_i \left[y_i \ln \left(\sum_j c_{ij}\lambda_j \right) - \sum_j c_{ij}\lambda_j - \ln(y_i!) \right] \tag{2}$$

If the logarithm of the prior M is used to impose additional constraints on the solution, we can compute the maximum-a-

K. Baete, J. Nuyts and P. Dupont are with the Department of Nuclear Medicine, University Hospital Gasthuisberg, B-3000 Leuven, Belgium (e-mail: kristof.baete@uz.kuleuven.ac.be). This work was supported by grant IDO-99/005.

W. Van Paesschen is with the Department of Neurology, University Hospital Gasthuisberg, B-3000 Leuven, Belgium.

P. Suetens is with the Laboratory for Medical Image Computing, Radiology-ESAT/PSI, University Hospital Gasthuisberg, B-3000 Leuven, Belgium.

posteriori (MAP) estimator of λ_j, given by

$$\Lambda = \arg\max_{\Lambda}(L + M) \tag{3}$$

A mathematical formulation of the attenuation of photons and the finite detector resolution effect is included in the system matrix, given by

$$c_{ij} = \sum_q \tilde{c}_{qj} a_q h_{iq} \tag{4}$$

where

$$a_q = \exp\left(-\sum_k l_{qk}\mu_k\right), \quad h_{iq} = \frac{1}{\sqrt{2\pi}\sigma}\exp\left(-\frac{d_{iq}^2}{2\sigma^2}\right)$$

with μ_k the linear attenuation coefficient at voxel position k, l_{qk} the effective intersection length of the projection beam through detector pair q with the volume represented by voxel k, h a shift-invariant Gaussian resolution blurring kernel with σ the standard deviation of the point spread function, proportional to the full width at half maximum (FWHM), d_{iq} the distance between detector sampling grid location i and q, and $\tilde{c}_{qj}$ the detection probability in absence of attenuation and detector resolution effect. We will ignore scatter and randoms in the theoretical framework of this paper.

Next, we define a number of subsets of the voxel space $\mathbb{J} = \{j \,|\, j = 1, \ldots, J\}$. These subsets are based on the anatomical information included in the segmentation images. The first set $\mathbb{B}$ corresponds to voxels belonging to the brain. The second set, complementary to $\mathbb{B}$, is denoted $\mathbb{O}$. These sets are defined by

$$\mathbb{B} = \{j \in \mathbb{J} \,|\, f_j^G + f_j^W + f_j^C > \epsilon_1\} \tag{5}$$

$$\mathbb{O} = \mathbb{J} \setminus \mathbb{B} \tag{6}$$

with $0 < \epsilon_1 \ll 1$. Set $\mathbb{B}$ is partitioned in voxels that are classified as voxels containing at least partially GM, denoted by $\mathbb{G}$. The complementary part of $\mathbb{G}$ within $\mathbb{B}$ is denoted by $\mathbb{N}$:

$$\mathbb{G} = \{j \in \mathbb{B} \,|\, f_j^G > \epsilon_2\} \tag{7}$$

$$\mathbb{N} = \mathbb{B} \setminus \mathbb{G} \tag{8}$$

with $0 < \epsilon_2 \ll 1$. Finally, two subsets within $\mathbb{N}$ are defined containing voxels which are composed of mainly WM, denoted by $\mathbb{W}$, and voxels composed of mainly CSF, denoted by $\mathbb{C}$:

$$\mathbb{W} = \{j \in \mathbb{N} \,|\, f_j^W \geq (1 - \epsilon_3)\} \tag{9}$$

$$\mathbb{C} = \{j \in \mathbb{N} \,|\, f_j^C \geq (1 - \epsilon_4)\} \tag{10}$$

with $0 < \epsilon_3, \epsilon_4 \ll 1$. Apart from these subsets, every PET voxel j can be thought of as a source with an activity λ_j equal to the total amount of fractional activities of the contributing tissues, or

$$\lambda_j = f_j^G\lambda_j^G + f_j^W\lambda_j^W + f_j^C\lambda_j^C + f_j^O\lambda_j^O \tag{11}$$

For $j \in \mathbb{G}$, we make an approximation of (11). Since both WM and CSF are expected to have a uniform activity, we can replace the activity of these tissues in (11) with their mean activities calculated in regions $\mathbb{W}$ and $\mathbb{C}$ respectively. Furthermore, GM is surrounded by WM and CSF, which implies that $f_j^O = 0$. For $j \in \mathbb{G}$, equation (11) is approximated by

$$\lambda_j \approx f_j^G\lambda_j^G + f_j^W\bar{\lambda}^W + f_j^C\bar{\lambda}^C \tag{12}$$

with

$$\begin{aligned} \bar{\lambda}^W &= \frac{1}{n_{\mathbb{W}}}\sum_{l\in\mathbb{W}} f_l^W\lambda_l, & n_{\mathbb{W}} &= \sum_{l\in\mathbb{W}} f_l^W, \\ \bar{\lambda}^C &= \frac{1}{n_{\mathbb{C}}}\sum_{l\in\mathbb{C}} f_l^C\lambda_l, & n_{\mathbb{C}} &= \sum_{l\in\mathbb{C}} f_l^C. \end{aligned} \tag{13}$$

In (13), we assume that λ_j represents the "true" value for WM and CSF. This assumption can be made if ϵ_3 and ϵ_4 in (9) and (10) are very small, which implies that we use only voxels which are "almost" homogeneous in a certain tissue class. Then, instead of estimating $\Lambda = \{\lambda_j \,|\, j \in \mathbb{J}\}$, we estimate Λ^*, with

$$\Lambda^* = \{\lambda_j^G \,|\, j \in \mathbb{G}\} \cup \{\lambda_j \,|\, j \in \mathbb{N} \cup \mathbb{O}\} \tag{14}$$

This can be considered as a transformation,

$$\begin{aligned} \forall j \in \mathbb{N} \cup \mathbb{O} : \lambda_j &\longrightarrow \lambda_j = \lambda_j \\ \forall j \in \mathbb{G} : \lambda_j &\longrightarrow \lambda_j^G = \frac{\lambda_j - f_j^W\bar{\lambda}^W - f_j^C\bar{\lambda}^C}{f_j^G} \end{aligned} \tag{15}$$

This is equivalent to a MAP reconstruction, presented in (3), if we replace c_{ij} by c_{ij}^* and λ_j by λ_j^*:

$$\begin{aligned} c_{ij}^* &= \delta_j^{\mathbb{G}} c_{ij} f_j^G + \delta_j^{\mathbb{W}} \frac{f_j^W}{n_{\mathbb{W}}} \sum_{k\in\mathbb{G}} c_{ik} f_k^W \\ &\quad + \delta_j^{\mathbb{C}} \frac{f_j^C}{n_{\mathbb{C}}} \sum_{k\in\mathbb{G}} c_{ik} f_k^C + \delta_j^{\mathbb{O}} c_{ij} + \delta_j^{\mathbb{N}} c_{ij} \end{aligned} \tag{16}$$

$$\lambda_j^* = \delta_j^{\mathbb{O}}\lambda_j + \delta_j^{\mathbb{N}}\lambda_j + \delta_j^{\mathbb{G}}\lambda_j^G \tag{17}$$

with

$$\delta_l^{\mathbb{X}} \equiv \begin{cases} 1 & \Longleftrightarrow \quad l \in \mathbb{X} \\ 0 & \Longleftrightarrow \quad l \notin \mathbb{X} \end{cases} \tag{18}$$

In $\mathbb{W}$, we impose a priori knowledge using a Gaussian prior, since $\mathbb{W}$ contains voxels composed of mainly WM which is expected to have a uniform activity. This is done similarly for voxels within $\mathbb{C}$ and $\mathbb{R} = \mathbb{N} \setminus (\mathbb{W} \cup \mathbb{C})$:

$$M_j^{\mathbb{W}} = -\delta_j^{\mathbb{W}}\beta_W \frac{(\lambda_j - \bar{\lambda}^W)^2}{2\sigma_W^2} \tag{19}$$

$$M_j^{\mathbb{C}} = -\delta_j^{\mathbb{C}}\beta_C \frac{\lambda_j^2}{2\sigma_C^2} \tag{20}$$

$$M_j^{\mathbb{R}} = -\delta_j^{\mathbb{R}}\beta_R \frac{(\lambda_j - f_j^W\bar{\lambda}^W)^2}{2\sigma_R^2} \tag{21}$$

with β_W, β_C, β_R the weights and σ_W, σ_C, σ_R the widths of the Gaussian priors. Note that $\mathbb{R}$ contains voxels partly composed of WM and CSF, and the WM accounts for the activity. The propagation of noise in $\mathbb{G}$ is controlled using a Gibbs smoothing prior, given by

$$M_j^{\mathbb{G}} = -\delta_j^{\mathbb{G}}\beta_g \sum_{k\in\mathcal{N}_j^{\mathbb{G}}} \frac{1}{d_{jk}}\Phi(\lambda_j^G, \lambda_k^G) \tag{22}$$

with β_g the prior weight, d_{jk} the Euclidean distance between voxel j and k, $\mathcal{N}_j$ the neighborhood of voxel j with $j \notin \mathcal{N}_j$ and $\mathcal{N}_j^{\mathbb{G}} = \mathcal{N}_j \cap \mathbb{G}$, and Φ the local prior weight based on a measure of the difference in activity at j and k. Then, we replace the logarithm of the prior in (3) with

$$M = M^{\mathbb{W}} + M^{\mathbb{C}} + M^{\mathbb{R}} + M^{\mathbb{G}} \tag{23}$$

Finally, the reconstruction image is computed via the inverse transformation described in (15). This means, for all $j \in \mathbb{G}$, λ_j^G should be replaced by

$$f_j^G \lambda_j^G + f_j^W \bar{\lambda}^W + f_j^C \bar{\lambda}^C \tag{24}$$

As in [4], we used a heuristic gradient ascent form of the expectation maximization (EM) approach for the optimization of (3). The iterative recontruction algorithm is then given by

$$\lambda_j^{n+1} = \lambda_j^n + \lambda_j^n \frac{\left.\frac{\partial L}{\partial \lambda_j}\right|_{\vec{\lambda}^n} + \left.\frac{\partial M}{\partial \lambda_j}\right|_{\vec{\lambda}^n}}{\sum_i c_{ij} - \lambda_j^n \left.\frac{\partial^2 M}{\partial \lambda_j^2}\right|_{\vec{\lambda}^n}} \tag{25}$$

Henceforth, this iterative reconstruction algorithm is called Anatomical based MAP (A-MAP).

III. Experiments

We studied the performance of this reconstruction algorithm for the detection of hypometabolic regions using a Monte Carlo simulation experiment.

Because the shape of the human brain is complex, we constructed a clinical realistic brain phantom. This phantom was based on the three-dimensional (3D) digital phantom provided by the *BrainWeb* database [5]. To speed up simulations, the experiment was performed on a two-dimensional (2D) transaxial slice. The digital phantom was used to make a baseline FDG-PET tracer distribution representing the glucose metabolism of a normal brain. We call this image, the baseline phantom (BP). For that purpose, the GM, WM and CSF tissues were identified in the discrete anatomical model [6], called: the binary tissue maps of GM, WM and CSF. The discrete BP was constructed by setting the activity to a clinical realistic number of 25 counts per voxel (cpv) in the GM region, 6.25 cpv in the WM region and 0 cpv in the CSF. Image dimensions are 217×217 voxels with an isotropic voxel size of 1 mm. In a duplicate of the BP, we selected five regions in the GM with a varying extent. The activity in these regions was decreased as in hypometabolic regions. This image is called: the hypometabolic phantom (HP). The extent E in voxel units and the proportional decrease of activity Δ of the regions are listed in Table I. Since, (a) our reconstruction method uses anatomical information in the form of tissue fractions, and (b) the anatomical information is assumed to be known exactly in the description of the experiment, both the discrete BP and HP were smoothed using a two-dimensional (2D) isotropic Gaussian kernel with 2 mm FWHM. The PET acquisition process was simulated by projection of both the BP and HP over 144 angles using a uniform attenuation image derived from the contour of the digital brain phantom and $\mu = 0.095\,\mathrm{cm}^{-1}$. To account for the finite resolution effect of the detector, both sinograms were smoothed along the detector grid using a one-dimensional (1D) Gaussian kernel with 5 mm FWHM. These sinograms were considered to be the noiseless PET measurements of the BP and HP. Of each sinogram a number of Poisson noise realizations were computed.

TABLE I

The extent E in voxel units and the proportional decrease Δ of activity for the hypometabolic regions.

region	extent E (voxels)	decrease Δ (%)
1	43	20
2	28	22
3	42	24
4	44	20
5	45	20

We studied the performance of the A-MAP algorithm in the detection of hypometabolic regions using the same anatomical information during reconstruction as for the construction of the phantoms. This means that the binary tissue maps of GM, WM and CSF were also smoothed using a two-dimensional (2D) isotropic Gaussian kernel with 2 mm FWHM and the different tissue fractions $\{f^G, f^W, f^C, f^O\}$ were determined. This is an ideal situation which enables us to study the optimal performance of using anatomical information.

The following reconstruction parameter settings were used for all three algorithms. The threshold parameters were $\epsilon_i = 0.01$, for $i = 1, 2, 3, 4$. In that way, all voxels with a partial GM contribution, i.e. at least $1\,\%$, are contained in $\mathbb{G}$. Moreover, voxels within $\mathbb{W}$ and $\mathbb{C}$ are almost homogeneously WM and CSF, respectively. The global weight of the smoothing prior was $\beta_g = 8$. The global weights of the Gaussian priors and their widths were $\beta_W = \beta_C = \beta_R = 10$ and $\sigma_W = \sigma_C = \sigma_R = 3$, respectively. The choice for Φ in the Gibbs prior of equation (22) was based on the following rationale. Since the normal glucose metabolism in the GM is not uniform but rather locally varying throughout the entire brain, the amount of penalty should not be based on the absolute, but rather on the relative difference of activities. Moreover, the penalization term should become tolerant for differences that are large enough to be real. We have recently shown that these properties are combined in the relative difference (RD) prior [4], in which

$$\begin{aligned} \Phi(x_j, x_k) &= \frac{(x_j - x_k)^2}{x_j + x_k + \gamma|x_j - x_k|} \iff k \in \mathcal{N}_j \\ &= 0 \iff k \notin \mathcal{N}_j \end{aligned} \tag{26}$$

with $\mathcal{N}_j$ a neighborhood of j and γ a parameter controlling the point from which the prior becomes tolerant. Penalization is quadratic for small and linear for large differences. The factor $2/\gamma$ is related to an "intermediate" relative difference value. We assumed that a relative difference of $5\,\%$ was an intermediate value, such that γ was set to 40.

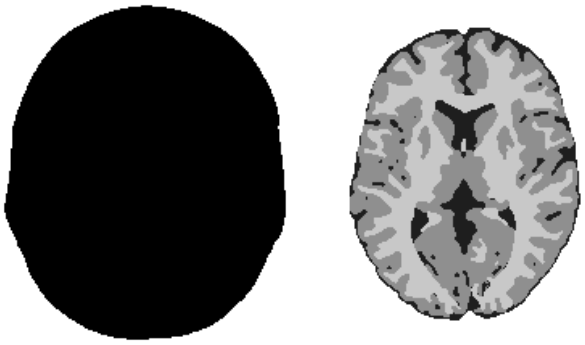

(a) (b)

Fig. 1. Figure (a) shows the uniform attenuation map. Figure (b) shows a composition of the binary tissue maps: CSF is indicated in black, GM in dark gray and WM in light gray.

The performance of the A-MAP algorithm was compared with post-smoothed ML-EM and MAP-EM. We used the post-smoothed ML-EM reconstruction algorithm as the current standard in this process of evaluation. This algorithm was implemented as described in (25), but with $M = 0$. The reconstruction image was post-smoothed using a two-dimensional (2D) isotropic Gaussian blurring kernel. The FWHM of this kernel was varied between 3 mm and 5 mm. We used the MAP-EM reconstruction algorithm as an indicator for the non-anatomical based use of prior information. The MAP-EM algorithm was implemented as described in (25) and

$$M = -\beta_g \sum_{k \in \mathcal{N}_j} \frac{1}{d_{jk}} \Phi(\lambda_j, \lambda_k) \tag{27}$$

where Φ is given by (26) and $\mathcal{N}_j$ a 3×3 neighborhood. Ordered subsets were used in all three algorithms. We used an iteration scheme with a decreasing number of subsets, consisting of (subsets $\times$ iterations): 36×5, 24×5, 18×5, 16×5, 12×5, 9×5, 8×5, 6×5, 4×5, 2×5, 1×10. This scheme is almost equivalent to 685 regular iterations.

Further, we use the following symbols: B^{nl} and H^{nl} for the reconstruction images of the noiseless PET emission data of BP and HP, respectively; $\lambda_j(B^{(r)})$ and $\lambda_j(H^{(r)})$ for the reconstruction images of noise realization r of the PET emission data of BP and HP, respectively. B^{ph} and H^{ph} denotes the "true" baseline and hypometabolic phantom images, respectively.

The performance of each algorithm was measured using a variety of metrics. The detection of hypometabolic regions was quantified using a computer observer. For each reconstruction algorithm and for each noise realization r, we measured

$$s_{\mathrm{nl}}(I^{(r)}, R) = \sum_{j \in R} (B_j^{\mathrm{nl}} - H_j^{\mathrm{nl}}) \cdot \lambda_j(I^{(r)}) \tag{28}$$

with I either B or H, and R a region of interest (ROI). For $s = s_{\mathrm{nl}}$, the signal-to-noise ratio (SNR) was computed using

$$\mathrm{SNR} = \sqrt{2 \frac{[\bar{s}(B) - \bar{s}(H)]^2}{\sigma_s^2(B) + \sigma_s^2(H)}} \tag{29}$$

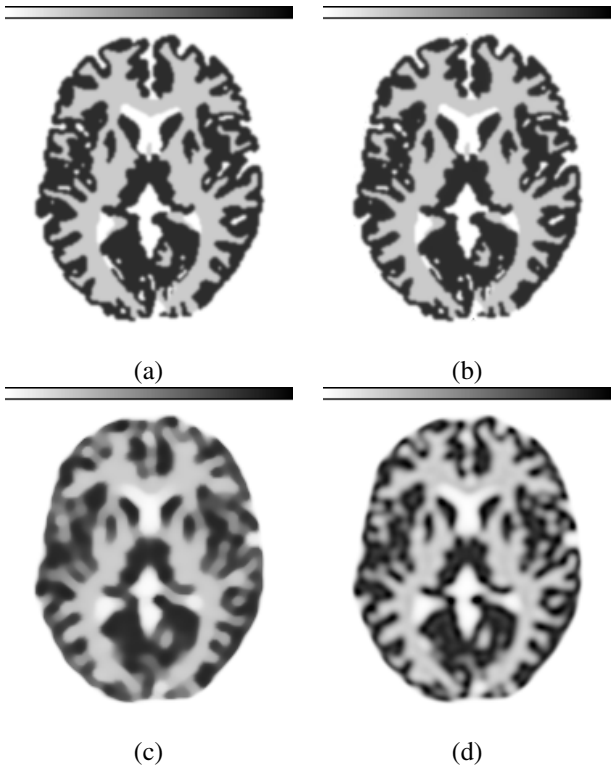

(a) (b) (c) (d)

Fig. 2. The baseline phantom (BP) image is shown in (a). The remaining figures show the reconstruction images of the noiseless BP emission data: the A-MAP reconstruction is shown in (b), the MAP-EM reconstruction is shown in (c) and the ML-EM reconstruction is shown in (d). All images are scaled to the same intensity range: white corresponds to zero and black corresponds to an activity of 30 counts per voxel.

with $\bar{s}(I)$ the mean and $\sigma_s^2(I)$ the variance of $s(I^{(r)})$ over all noise realizations. The root mean squared (rms) bias $\tilde{b}(I, R)$ in ROI R was computed using

$$\tilde{b}(I, R) = \sqrt{\frac{1}{n_R} \sum_{j \in R} \left(\bar{\lambda}_j(I) - I_j^{\mathrm{ph}} \right)^2} \tag{30}$$

with $\bar{\lambda}(I)$ the mean of $\lambda(I^{(r)})$ over all noise realizations, n_R the number of voxels in R, and I either B or H. The rms variance was computed using

$$\tilde{\sigma}^2(I, R) = \frac{1}{n_R} \sum_{j \in R} \frac{1}{P - 1} \sum_{r=1}^{P} \left(\lambda_j(I^{(r)}) - \bar{\lambda}_j(I) \right)^2 \tag{31}$$

with P the number of noise realizations. Finally, we measured the rms difference (RMSD) between image $[B^{\mathrm{ph}} - H^{\mathrm{ph}}]$ and image $[\bar{\lambda}(B) - \bar{\lambda}(H)]$ over different ROIs R.

IV. Results

The two-dimensional (2D) uniform attenuation image that was used in the experiments is shown in Fig. 1(a). For visualization purposes, a composition of the binary tissue maps of GM, WM and CSF was constructed and is shown in Fig. 1(b). The baseline phantom (BP) is shown in Fig. 2(a).

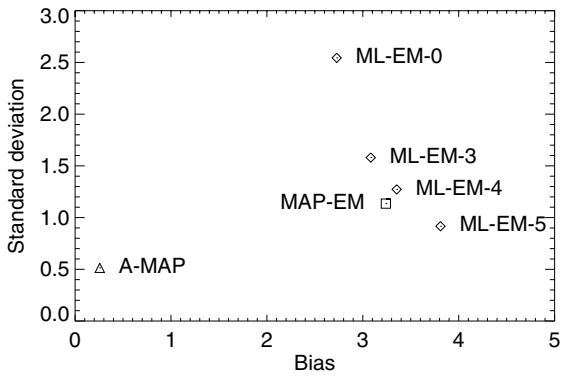

Fig. 3. The root mean squared (rms) bias $\tilde{b}(B, \mathbb{J})$ and the rms standard deviation $\tilde{\sigma}(B, \mathbb{J})$ of all reconstruction algorithms are shown in this diagram. ML-EM-X means post-smoothed ML-EM using a two-dimensional (2D) isotropic Gaussian kernel with X mm FWHM.

The A-MAP, using the exact anatomical information, the ML-EM and the MAP-EM reconstruction images of the noiseless PET emission data of the baseline phantom, B^{nl}, are shown in Fig. 2(b – d). We computed $P = 683$ Poisson noise realizations of the noiseless PET emission data of the BP and HP. The SNR and RMSD results for each reconstruction algorithm over different regions-of-interest are shown in Table II. The SNR values were scaled with respect to the SNR of the MAP-EM algorithm for comparison. The root mean squared (rms) bias and rms variance results of the reconstruction algorithms are shown in Fig. 3.

V. Discussion

We have presented an iterative reconstruction algorithm, tentatively called A-MAP, that was developed for the detection of hypometabolic regions in FDG-PET images of the brain of epilepsy patients. Prior knowledge was included in the reconstruction process, partly based on information derived from MR data and partly based on the underlying pathology. Note that the general structure of the iterative reconstruction algorithm, shown in 25, was not altered. The major change was made using a transformation of variables, which has a positive effect on the computational complexity of the algorithm.

A-MAP showed an improved SNR and a reduction of rms bias, compared to MAP-EM and post-smoothed ML-EM. We can consider bias to be an important parameter in the evaluation of this reconstruction algorithm, since, in clinical practice, only one (interictal) PET image is acquired. As opposed to e.g. subtraction SPECT imaging in epilepsy, there is no ictal counter image to compare with. The RMSD results reduced when using A-MAP.

VI. Conclusion

We derived an iterative reconstruction algorithm, dedicated for the detection of small hypometabolic regions in FDG-PET images of the brain of epilepsy patients. Anatomical information and knowledge about the underlying pathology was included in the algorithm. Monte Carlo simulations showed an improved signal-to-noise ratio and reduced bias. We can conclude that the use of anatomical information combined with information about the underlying pathofysiology is very promising for the detection of hypometabolic regions in the brain of epilepsy patients. Further evaluation of the algorithm is underway.

TABLE II

The signal-to-noise ratio (SNR) and root mean squared difference (RMSD) results. The SNR results of A-MAP and ML-EM were relatively scaled with respect to the MAP-EM algorithm. ML-EM-X means post-smoothed ML-EM using a two-dimensional (2D) isotropic Gaussian kernel with X mm FWHM. Both the SNR and RMSD were computed over different regions-of-interest (ROI): $\mathbb{J}$, the whole image, and R_i, circular ROIs, with a ten voxel wide radius, centered at the location of the hypometabolic regions i.

Algorithm	SNR(s_{nl})					
	$\mathbb{J}$	R_1	R_2	R_3	R_4	R_5
A-MAP	1.25	1.26	1.17	1.30	1.23	1.33
MAP-EM	1.00	1.00	1.00	1.00	1.00	1.00
ML-EM-0	0.77	0.73	0.76	0.81	0.74	0.77
ML-EM-3	0.94	0.90	0.92	1.00	0.98	0.94
ML-EM-4	1.01	0.97	0.99	1.06	1.05	1.02
ML-EM-5	1.10	1.07	1.08	1.13	1.13	1.12
Algorithm	RMSD$\{[B^{\mathrm{ph}} - H^{\mathrm{ph}}], [\bar{\lambda}(B) - \bar{\lambda}(H)]\}$					
	$\mathbb{J}$	R_1	R_2	R_3	R_4	R_5
A-MAP	0.18	0.74	0.73	0.82	0.61	0.51
MAP-EM	0.23	0.92	0.87	0.89	0.74	0.73
ML-EM-0	0.20	0.72	0.67	0.64	0.50	0.56
ML-EM-3	0.21	0.81	0.75	0.80	0.68	0.64
ML-EM-4	0.22	0.86	0.79	0.91	0.78	0.70
ML-EM-5	0.24	0.94	0.86	1.05	0.91	0.81

VII. Acknowledgment

The authors wish to thank Dirk Vandermeulen, Siddharth Srivastava and Dirk Bequé for useful discussions regarding this study.

References

[1] K. Van Leemput, F. Maes, D. Vandermeulen, and P. Suetens, " Automated model-based tissue classification of MR images of the brain," *IEEE Trans. Med. Imag.*, vol. 18, No. 10, pp. 897 – 908, Oct. 1999.

[2] S. Sastry, and R.E. Carson, " Multimodality bayesian algorithm for image reconstruction in positron emission tomography: a tissue composition model," *IEEE Trans. Med. Imag.*, vol. 16, No. 6, pp. 750 – 761, Dec. 1997.

[3] F. Maes, A. Collignon, D. Vandermeulen, G. Marchal and P. Suetens, " Multimodality image registration by maximization of mutual information," *IEEE Trans. Med. Imag.*, vol.16, no. 2, pp. 187 – 198, Apr. 1997.

[4] J. Nuyts, D. Bequé, P. Dupont and L. Mortelmans, " A concave prior penalizing relative differences for maximum-a-posteriori reconstruction in emission tomography," *IEEE Trans. Nucl. Sci.*, vol. 49, No. 1, pp. 56 – 60, Feb. 2002.

[5] http://www.bic.mni.mcgill.ca/brainweb

[6] D.L. Collins, A.P. Zijdenbos, V. Kollokian, J.G. Sled, N.J. Kabani, C.J. Holmes, and A.C. Evans, " Design and construction of a realistic digital brain phantom," *IEEE Trans. Med. Imag.*, vol. 17, No. 3, pp. 463 – 468, Jun. 1998.